Spreading resistance effects in tunneling spectroscopy of α-$RuCl_3$ and $Ir_{0.5}Ru_{0.5}Cl_3$

Jordan R. Frick,[1] Samanvitha Sridhar,[1] Ario Khansari,[1] Andrew H. Comstock,[1] Elizabeth Norman,[1] Shaun O'Donnell,[2] Paul A. Maggard,[2] Dali Sun,[1] and Daniel B. Dougherty[1,*]

[1]*Department of Physics, North Carolina State University, Raleigh, North Carolina 27695, USA*

[2]*Department of Chemistry, North Carolina State University, Raleigh, North Carolina, 27695, USA*

(Received 14 March 2022; revised 13 July 2023; accepted 1 November 2023; published 12 December 2023)

The Mott insulating state is the progenitor of many interesting quantum phases of matter including the famous high-temperature superconductors and quantum spin liquids. A recent candidate for novel spin liquid phenomena is α-$RuCl_3$, a layered honeycomb Mott insulator whose electronic structure has been a source of mystery. In particular, scanning tunneling spectroscopy has indicated a Mott gap in α-$RuCl_3$ that is much lower than the 2-eV value observed in photoemission measurements. Here, we show that the origin of this discrepancy is a spreading resistance artifact associated with tunneling into highly resistive materials by comparing with prior experiments and numerical modeling. A similar phenomenon is also observed in a substitutional alloy, $Ir_{0.5}Ru_{0.5}Cl_3$, that has a higher resistivity than the parent compound. While the tunneling measurements cannot be used to accurately measure the sample density of states for these materials, we can take advantage of the spreading resistance sensitivity to quantify the anisotropic resistivity of these layered materials and connect to previous macroscopic transport observations.

DOI: 10.1103/PhysRevB.108.245410

I. BACKGROUND

The spin-orbit assisted Mott insulator, α-$RuCl_3$, is an important example of the "strong-Mott" regime of spin-orbit (SO) coupled quantum matter [1]. It has a large Mott gap of $\sim$2 eV that arises from the concerted impact of electronic repulsion and SO coupling [2]. Carriers are localized on atomic sites, leading to charge transport via thermally activated or variable range hopping. The strong insulating character has potential device applications due to a pinched hysteresis in its *I-V* curve, making it a promising memristor material for neuromorphic computing applications [3]. It has also been explored as a potential Kitaev quantum spin liquid material [2,4,5] and it has long-lived Mott-Hubbard excitons [6]. Exploration of each of these interesting phenomena requires quantitative observation of the electronic structure of the material.

The complexity of the Mott insulating state in SO-coupled materials can be elaborated upon by considering elemental substitution within $RuCl_3$ crystals. For example, Ir^{3+} substitution in $RuCl_3$ could enhance SO coupling effects due to the larger effective nuclear charge and thus move the substituted material further into the poorly explored strong Mott regime of SO-coupled matter [1]. Furthermore, a significant impact of Ir substitution on magnetic ordering properties in compounds of the generic form $Ir_xRu_{1-x}Cl_3$ has been observed. In particular, Ir^{3+} substitution above the percolation threshold of $x = 0.2$-0.3 shows evidence of dominant fractionalized excitations indicative of a quantum spin liquid [7–9]. All of these effects depend sensitively on the basic electronic structure of the parent Mott insulator.

In α-$RuCl_3$, spin-orbit coupling causes a splitting of the of the t_{2g} orbitals into $j_{1/2}$ and $j_{3/2}$ subbands [2]. The $j_{1/2}$ subband is half filled and thus would be metallic; however, strong electronic repulsions in the 4*d* orbitals cause it to split into an upper Hubbard band (UHB) and lower Hubbard band (LHB). The charge gap of $\sim$2 eV in α-$RuCl_3$ has been directly measured by a combination of ultraviolet and inverse photoelectron spectroscopy and modeled using a combination of cluster-based and density-functional theory (DFT) $+U$ calculations [10]. In addition, detailed optical spectroscopy studies have assigned the so-called β peak to free carrier photoexcitations at $\sim$2-eV excitation energy [11]. Our recent time-resolved two-photon photoemission experiments access this excitation and also place the UHB at about 2 eV above the LHB [6].

Despite this general agreement about the size of the Mott gap, there is an anomaly reported based on scanning tunneling spectroscopy (STS). These measurements [12] identify a gap that is much smaller than found through DFT calculations [2] and photoemission experiments [6,10], and this observation is noted as a fundamental problem. Scanning tunneling spectroscopy has a long history of application to the study of gaps in semiconductors [13,14]. However, often substantial care must be taken to address measurement sensitivity [14] and artifacts such as tip-induced band bending [15,16] and spreading resistance effects [17].

In this work, we resolve the $RuCl_3$ gap discrepancy in STS by identifying strong spreading resistance effects. We have found that the anomalously small apparent gap is an artifact of the insulating character of $RuCl_3$ that allows spreading resistance to dominate the tunneling measurements. While

*dbdoughe@ncsu,edu

this artifact obscures the intrinsic electronic properties, it can instead be used to explore the nanoscale transport properties of the Hubbard bands [17]. We show that these effects are enhanced in $Ir_{0.5}Ru_{0.5}Cl_3$ due to its higher resistivity and discuss the implications of this comparison in the context of transport properties of SO-coupled quantum materials.

II. EXPERIMENTAL METHODS

Single crystals of α-$RuCl_3$ were prepared using chemical vapor transport as described previously [18]. Solid solutions of $Ir_{0.5}Ru_{0.5}Cl_3$ were prepared by loading stoichiometric mixtures of $IrCl_3$ and $RuCl_3$ powders (Millipore-Sigma, as received) in quartz ampoules that were evacuated, sealed, and loaded into a box furnace. The Ir-substituted $RuCl_3$ crystal-growth procedure was identical to the pure $RuCl_3$ growth. This material is of interest in its own right, as mentioned in the introduction [9], but also serves as a control sample with different transport properties but a similar density of states compared to $RuCl_3$.

Imaging and local spectroscopy experiments were carried out in an ultrahigh-vacuum (UHV) scanning tunneling microscopy (STM) system with a base pressure of 1×10^{-10} Torr. Samples were cleaved in air and immediately introduced to the UHV system. Ultraviolet photoelectron spectroscopy measurements were carried out with identical sample preparation procedures in a separate UHV system (base pressure $\sim 2 \times 10^{-10}$ Torr) housing a He discharge lamp photon source (Specs UVS 10/35) and a commercial hemispherical electron spectrometer with 2D charge-coupled device detector (Specs Phoibos 150). Fermi levels referenced in these spectra correspond to the standard detector work function calibration.

Scanning tunneling microscopy and spectroscopy experiments were performed with both chromium and tungsten tips. The samples were held at ambient temperature during imaging in a commercial STM instrument (Omicron VTSTM-XA). Local differential tunneling conductance was measured with standard lock-in techniques (10-kHz modulation frequency, ~0.1-V rms amplitude) that we have used successfully in the past [19,20]. The modulation amplitude is somewhat larger than used for typical STS studies but small compared to the expected $RuCl_3$ Mott gap and comparable to the expected thermal broadening of the tip Fermi function. Capacitive signals were minimized by adjusting the phase of the lock-in amplifier to be 90° from the phase for which the signal was maximized with the tip just outside of tunneling range. The crucial STS observations were carried out by measuring local tunneling spectra at different starting setpoint currents with the voltage setpoint at +0.6 V. The choice of starting setpoint current determines the height of the STM tip above the surface during the STS measurement and thus the resistance of the tunneling gap.

A numerical model of the impact of spreading resistance on tunneling current-voltage curves was used to verify that the key observational features of this effect can be produced by a simple series resistor model. This model adapts aspects of several prior numerical studies of tunneling spectroscopy [21–23] to the case when the spreading resistance adds a nonzero series contribution to the tunneling resistance. This establishes a voltage divider with a strongly nonlinear tunneling resistance that must be addressed numerically. The details of the model and sample PYTHON scripts are included in the Supplemental Material [24].

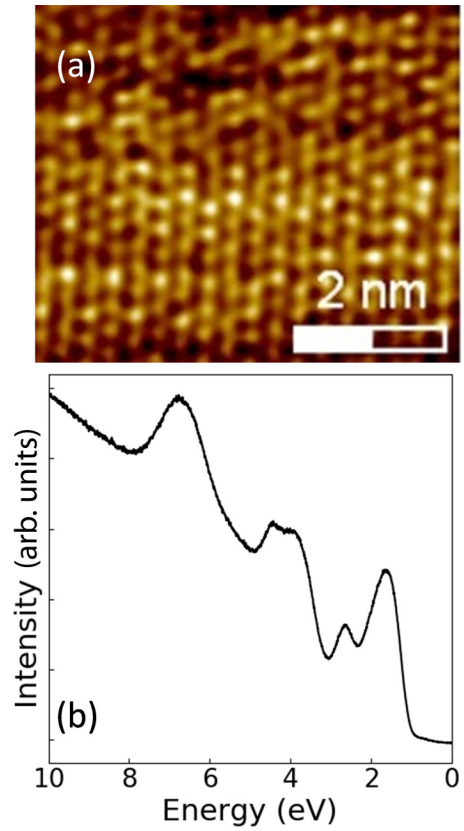

FIG. 1. (a) Atomically resolved STM image of a cleaved α-$RuCl_3$ surface (0.6-V bias, 60 pA); (b) UPS spectra of α-$RuCl_3$ showing the occupied states.

For bulk two-contact resistivity measurements, gold wires were attached with Epotek Ag epoxy directly to crystals of $RuCl_3$ and $Ir_{0.5}Ru_{0.5}Cl_3$ with the sample held in ambient air as described in the original transport studies of $RuCl_3$ [25]. The two-contact sample geometry was measured with calipers and optical microscope inspection to be approximately 156 μm in length, 100 μm in thickness, and 1.78 mm in width for $RuCl_3$. The geometry for $Ir_{0.5}Ru_{0.5}Cl_3$ was 822 μm in length, 350 μm in thickness, and 2.59 mm in width. The sample resistance between the two epoxy contacts was measured using a Quantum Design Physical Property Measurement System and resistivity calculated by assuming a rectangular parallepiped sample geometry even though the epoxy contacts were somewhat irregular in shape. The sample temperature was lowered until the resistance measured was higher than the system's upper measurement limit (~2 GΩ).

III. RESULTS

Figure 1(a) shows an atomically resolved STM image of an α-$RuCl_3$ crystal where the expected spacing between features is ~0.3 nm, in agreement with prior STM imaging studies [12]. In addition, some surface defects exist but we have not carried out a systematic study of their ori-

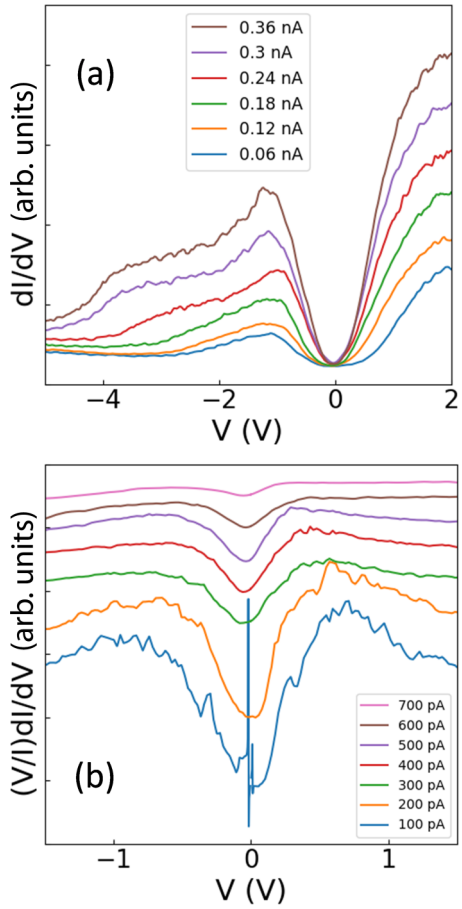

FIG. 2. (a) Tunneling conductance averaged over a 50-nm × 50-nm region at different setpoint currents; (b) Normalized tunneling conductance over a larger range of initial tunneling setpoints than in part (a) that shows the collapse of the apparent Mott gap as the tip approaches the surface. From bottom to top the spectra correspond to 0.1-, 0.2-, 0.3-, 0.4-, 0.5-, 0.6-, and 0.7-nA setpoint currents.

gin. Figure 1(b) shows a UPS spectrum where the lower Hubbard band of α-$RuCl_3$ is clearly resolved with an onset at ∼1-eV binding energy and a main peak at ∼1.3 eV. This spectrum agrees with previous observations from photoemission experiments on α-$RuCl_3$ [10,26]. However, when we measure the local density of states with STS conductance spectroscopy as shown in Fig. 2(a), there is a discrepancy. In conductance measurements, the onset and peak center of the LHB occur at energies much closer to the Fermi energy than in photoemission measurements. Similarly, the UHB on the positive side of zero is also at much lower energy than in previous inverse or two-photon photoemission measurements [6,10]. However, tunneling conductance also includes as a background signal the strongly voltage-dependent tunneling transmission function and is thus not a perfectly accurate measure of sample density of states except for very low bias. This can be corrected by detailed modeling [21,23], preprogrammed variable height measurements [14], or by using the empirical observation that dividing differential conductance by *I/V* approximately factors out the effects of the transmission function [13]. Such a normalized tunneling conductance for $RuCl_3$ is shown in Fig. 2(b) for a range of initial setpoints larger than in Fig. 2(a). When the normalization is applied, the anomalously small gap is even more obvious than in the raw conductance. Nevertheless, it is important to bear in mind that normalized tunneling conductance is a useful tool for accurate extraction of *peaks* in the density of states but *not* for the extraction of band-edge positions near a gap. This is because the tunneling transmission function does not vanish inside a gap even though the current and conductance both do. As a result, the (*V/I*) normalization does not accurately factor the transmission function out of the conductance in this region and empirical broadening must often be applied to make sense of gap sizes [27].

In addition to the smaller than expected Mott gap, the feature that might be associated with the LHB in Fig. 2(a) is evidently substantially broadened. The general asymmetric shape is similar to the UPS data in Fig. 1(b), but the higher binding energy shoulder is progressively expanded and shifted away from 0 V as the tunneling current setpoint increases, similar to prior reports for Mott insulating surface reconstructions studied by STS [17,28]. Looking ahead, we will argue in this paper that the unusual data in Fig. 2 do *not* probe the local density of states of the sample, even when normalized, since the measured current has significant contributions from processes other than tunneling.

Discrepancies between the charge gaps of semiconductors measured by STS compared to other techniques are common but are expected to go in the opposite direction than we report here for α-$RuCl_3$. On one hand, minor gap overestimation can result from the fact that accurate extrapolation of band edges is difficult in fixed height measurements due to the low signal to noise in the gap. Variable height measurements can help solve this issue and have been applied to traditional semiconductors [14] and more recently to transition-metal dichalcogenides [29].

Another source of gap overestimation arises from tip-induced band-bending (TIBB) effects and tend to make the effective gap somewhat larger in tunneling experiments due to the large electrostatic field (∼1 V/nm) applied between the tip and the sample. In semiconducting materials, applied fields are inefficiently screened due to a low density of free carriers and can bend the electronic bands away from the middle of the gap. In fact, TIBB effects have recently been reported for La-doped Sr_2IrO_4, a spin-orbit assisted Mott insulator similar to α-$RuCl_3$ [30]. In this material, the charge gap measured by STS is significantly larger than the expected gap of 0.6 eV and the apparent gap is observed to increase as the tunneling setpoint current increases.

By contrast for $RuCl_3$, the gap around zero bias appears to get smaller in our conductance measurements as the current setpoint increases. However, there is also evidence of possible TIBB in the tunneling spectra in the form of a shift in the tail of the occupied feature in Fig. 2(a). This asymmetric feature in the occupied density of states moves by several electron-volts. The situation for α-$RuCl_3$ combining an anomalously small apparent gap that shrinks with increasing setpoint with TIBB effects farther from zero bias has also been reported for another Mott insulator: the (3 × 3)-Si surface reconstruction of SiC(0001) [17]. The study describing this surface attributed the unusual behavior of spectral features in STS to spreading resistance artifacts. Based on the similarity to this prior report,

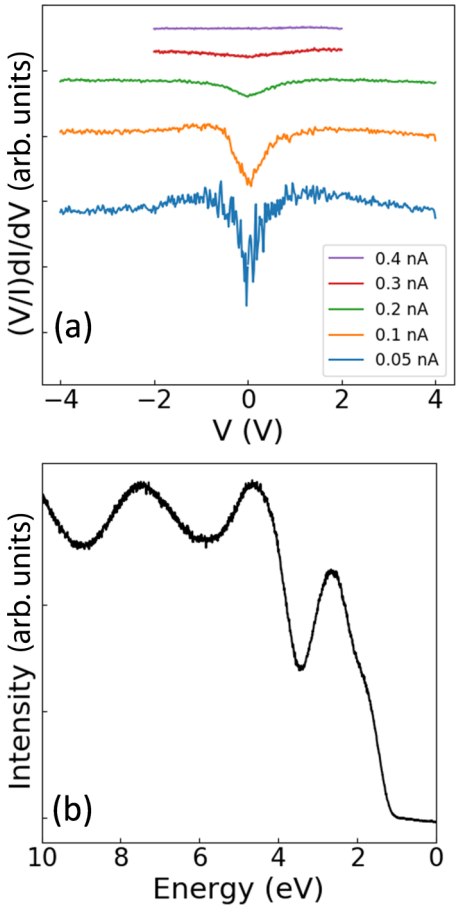

FIG. 3. (a) Averaged normalized dI/dV spectra of $Ir_{0.5}Ru_{0.5}Cl_3$ showing an even stronger dependence on tunneling setpoint current than for $RuCl_3$. (b) UPS spectrum of $Ir_{0.5}Ru_{0.5}Cl_3$ indicating the presence of a significant gap.

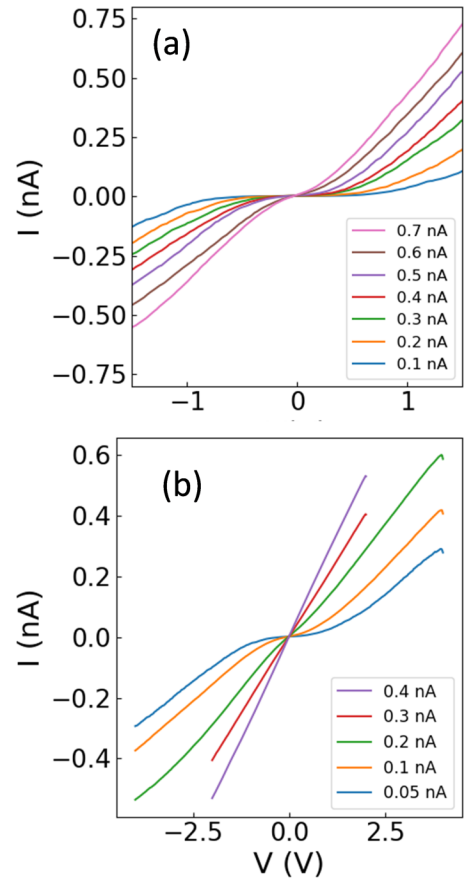

FIG. 4. (a) Averaged *I-V* spectra of α-$RuCl_3$ at different tunneling setpoint currents corresponding to Fig. 1(d) showing a linearization at high setpoint. (b) Averaged *I-V* spectra corresponding to Fig. 2(a) of $Ir_{0.5}Ru_{0.5}Cl_3$ showing an even stronger dependence on tunneling setpoint current.

we also ascribe our observations in Fig. 2 to spreading resistance artifacts and provide further evidence and discussion in what follows.

In our experiments on α-$RuCl_3$, increasing the initial setpoint current can result in an apparent collapse of the charge gap. This effect can be seen in the normalized conductance spectra in Fig. 2(b). In this sequence, the normalization makes clear that under no circumstance can a clear gap be extracted from the data since it always exhibits a V shape reminiscent of a semimetal. The apparent V shape in the normalized conductance becomes substantially less pronounced as the setpoint increases, though the details of the tunneling current dependence are sensitive to the specific STM probe tip in use. However, regardless of STM tip state, the observed gaps are always smaller than the expected 2 eV and can be made to approach zero at large enough tunneling current setpoints.

When the same experiment is performed on $Ir_{0.5}Ru_{0.5}Cl_3$ solid solutions, these effects are much more apparent as seen in Fig. 3(a). The onset of the tunneling conductance occurs at around 0 V even at very small tunneling setpoints. In Fig. 3(b), the lowest-energy occupied band of the substitutional alloy measured by UPS has a different shape than in pure $RuCl_3$ but the onset of the occupied band is around 1.2 eV below zero. This implies a charge gap of at least about 1 eV. The STS data in Fig. 3(a) show only a very small gap at low setpoints and by 400 pA the dI/dV spectra appear completely flat with no suppression near zero bias at all, which is very surprising in what is supposed to be a tunneling measurement. This is the same general discrepancy as for α-$RuCl_3$ but apparently more severe for the substitutional alloy with Ir.

The results shown in Figs. 1–3 all point to the particular artifact associated with in-plane spreading resistance in high-resistivity materials [17] that means charge motion is not only via tunneling, and conductance is thus not simply related to the sample density of states. This is further emphasized by the data in Fig. 4. Figure 4(a) shows the *I-V* curves measured simultaneously with the conductance data in Fig. 2(b), (and used to construct the normalized spectra). We note that particularly at positive biases, the curve becomes progressively more linear as the current setpoint is increased. This is another signature of spreading resistance effects as described in more detail in the next section. Once again, the situation is more apparent for $Ir_{0.5}Ru_{0.5}Cl_3$ as shown in Fig. 4(b), where the linearity is nearly perfect and more symmetrical about zero bias.

To better understand the comparison between the two materials, Fig. 5(a) shows the bulk resistance as a function of temperature for $RuCl_3$ and $Ir_{0.5}Ru_{0.5}Cl_3$. The higher values

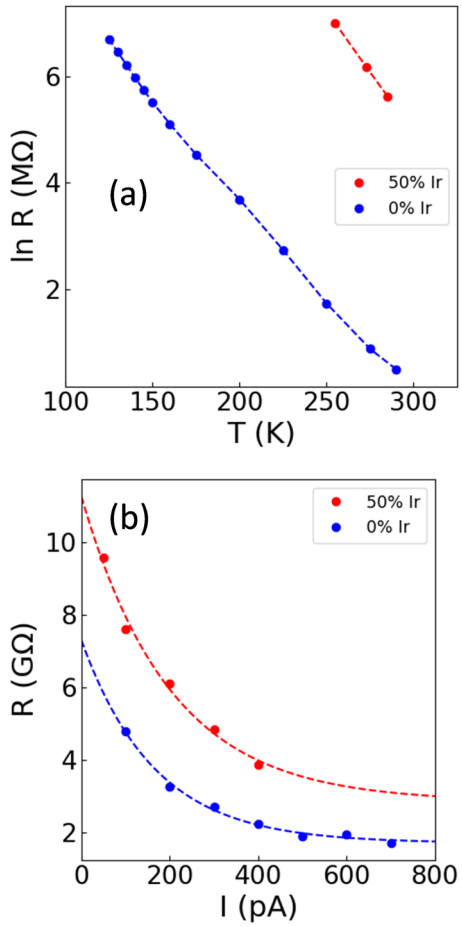

FIG. 5. (a) Bulk sample resistance as a function of temperature for pure $RuCl_3$ and $Ir_{0.5}Ru_{0.5}Cl_3$. (b) Tip-sample resistance as a function of tunneling setpoint current extracted from Figs. 4(a) and 4(b), showing a decrease in the total resistance of the tip-vacuum-sample system. An exponential fit is fit to the trend to extract a value for the spreading resistance.

for the substitutional alloy are consistent with the idea that spreading effects are dominant in tunneling experiments. Importantly, in highly resistive materials such as considered here, tunneling spectroscopy is no longer an accurate tool for measuring density of states. However, it may instead provide some insights about charge transport, and both of these points are discussed in the next section.

IV. DISCUSSION

A. Spreading resistance implications for STS

In this section, we discuss the rationale for assigning the observed tunneling spectra to spreading resistance artifacts. Very similar behavior to our observations has been reported before for a Mott insulating surface of Si-(3 × 3)-6H-SiC(0001). First, Ramachandran and Feenstra described broadening effects in their attempts to carry out STS of this surface [28] which, like $RuCl_3$, did not agree with prior photoemission studies. Later, Baffou *et al.* [17] returned to this system to quantify the high resistance of transport through the upper and lower Hubbard bands and connect with luminescence measurements. They noted an increasing linear character to the *I-V* curves as the initial setpoint is increased, as well as an asymmetry and some apparent broadening effects in the deeply bound parts of the tunneling spectra similar to our Figs. 1–3. The origin of the empirical broadening signature can be qualitatively attributed to the interplay between a quasilinear current-voltage characteristic due to spreading resistance with the highly nonlinear characteristic due to tunneling, as will be discussed in more detail in our numerical model results below. This has the effect of stretching spectral features if the spreading effect is weak, and dominating over the density of states when it is strong. In addition, spreading resistance involves long-range electrostatics [31] compared to tunneling and thus a samples a relatively large surface region [32,33].

An alternative explanation of the unusual spectra for the case of the (3 × 3)-Si surface was proposed by Gasparov *et al.*, who tentatively attributed the broadening to hybridization of tip states with the Hubbard band edges [34]. However, Baffou *et al.* noted that this explanation is not consistent with high-bias linearity in the *I-V* curves in this system [17] that we also observe for $RuCl_3$. Additional rejected interpretations for the spectra in Figs. 1–3 include a thermal metal-insulator transition due to Joule heating that would require temperatures that would irreversibly decompose the sample [35]. Alternately, vibration-assisted tunneling can lead to some small broadening of spectra as the tip approaches the sample [36]. However, this also results in a negative differential resistance signature that we did not observe. As a result, we favor the spreading resistance interpretation for the observed anomalous tunneling current behavior shown in Figs. 1–3.

A phenomenological model of how spreading resistance effects arise has been proposed [37] by partitioning the total resistance (R) of the tunneling system into a combination of the tunneling resistance (R_T), the sample resistance (R_S), and the spreading resistance (R_{SP}) just below the tip according to

$$R = R_T + R_S + R_{SP}. \tag{1}$$

In this expression, R_{SP} is present due to the need for charge transport away from the injection point directly under the tip. In most samples studied by STM methods, the sample and spreading resistance will be much lower than the tunneling resistance and can be neglected. For highly resistive samples, this approximation breaks down. If R_S is large enough, the injected charge from the tip will not be able to move away easily, causing a large voltage drop near the tip. This can make it so that R_{SP} and/or R_S can be comparable to R_T. Furthermore, by raising the tunneling setpoint current while keeping the tip-sample bias constant, the tip-to-sample distance is lowered. This also has the effect of lowering the tunneling resistance. For a highly resistive sample with a small tip-sample distance, the STS spectra are no longer simply related to the local density of states of the surface. Moreover, the effects of spreading resistance are less spatially localized than vacuum tunneling and thus tend to degrade high-resolution imaging capabilities. In fact, despite the occasional atomic resolution such as seen in Fig. 1(a), we found STM imaging quality of $RuCl_3$ to be generally poor, indicative of degraded spatial resolution expected in systems with strong spreading resistance effects.

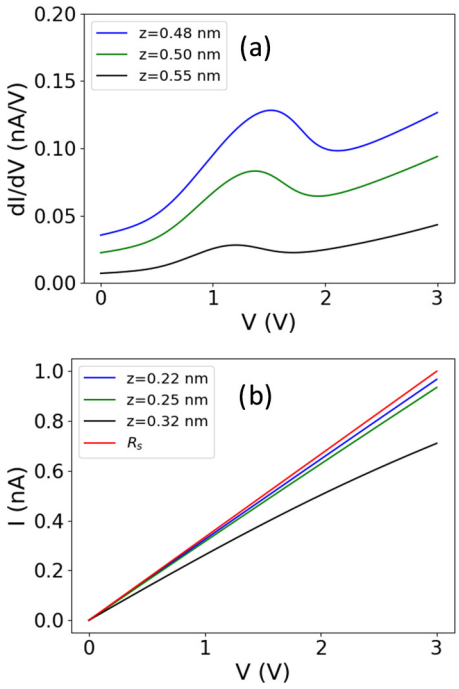

FIG. 6. (a) Differential conductance for different tip-sample distances showing how distortion of a peak structure is increased as the distance decreases when spreading resistance is included; (b) Extremely small tip-sample distances that show tunneling $I(V)$ curves where essentially no remnant of the sample DOS can be observed but where the slope tends to approach the spreading resistance value R_s.

Connection to the observations here and in prior experiments on related materials [17,28] can be made by a numerical study of the series resistor model in Eq. (1) with only R_{SP} considered. Intuitively, if both series resistors were of fixed value, independent of applied voltage across the network, the voltage divider effect would rigidly shift any density of states (DOS) features in the tunneling resistance to higher bias. However, the modeling challenge is that the tunnel junction is a strongly voltage-dependent resistor so that a nonlinear voltage divider equation (see Supplemental Material [24]) needs to be solved numerically to extract the potential difference that appears across the junction. This is the origin of the complex phenomenology observed in STS experiments with significant spreading resistance artifacts.

Figure 6(a) shows simulated differential conductance using an assumed density of states with a Gaussian peak at 1.0 eV, a half width of 0.4 eV, and a spreading resistance of 3 GΩ [24]. The peak feature in the dI/dV curve is strongly asymmetric in a way that goes beyond expected transmission function effects (see Supplemental Material for detailed comparisons). The intuition is that as the tunneling junction reaches a bias that starts to include the DOS peak from the low-voltage side, the resistance of the junction drops and the fraction of total potential difference that appears across the junction also drops. This expands the apparent voltage window over which the leading edge of the peak develops and shifts the peak position to higher bias in line with naive intuition. Conversely, as the peak intensity falls off at larger voltage, more of the total voltage appears across the gap and the feature disappears abruptly.

This distortion of the DOS peak in the simulated dI/dV is similar to the "broadening" that we observe experimentally, e.g., in Fig. 1(a). In addition, the conductance at low biases near 0 V increases with current setpoint in our numerical model results. This can be also be seen from the increasing low-bias slope in the experimental *I(V)* curves in Fig. 4. Finally, by considering extremely small tunneling distances where spreading resistance dominates, we can confirm the expectation that the high-bias slope of the $I(V)$ curve approaches the value of the spreading resistance as shown in Fig. 6(b). Here the red curve of highest slope is Ohm's law expectation for a pure spreading resistance, and the other three curves show progressively smaller tip-sample distances where the high-bias slope approaches Ohm's law expectation from below. The combination of peak distortion and high-bias linearity are the key qualitative observational features to be explained by the numerical model. Precise quantitative modeling of the shape of $I(V)$ curves under these conditions would require detailed knowledge of the tip shape and properties (including possible bias-dependent barrier height [13]) that is almost impossible to obtain reliably. However, the numerical simulation supports the basic qualitative assertions about spreading resistance artifacts reported here and in previous work.

With this explanation and qualitative model, the anomalously small Mott gap in STS measurements of $RuCl_3$ is identified as a spreading resistance artifact. It is worth noting that this effect is particularly significant for the large-gap Mott insulators considered here but that substantial tunneling artifacts may also be relevant to other Mott insulators. For example, TIBB effects have been clearly identified for an iridate crystal [30] and some discrepancies in gap sizes have been discussed for other iridates [38,39]. In general, the study of bulk insulators by STM-based spectroscopic techniques needs to be approached with caution.

The specific case of layered or low-dimensional Mott insulators seems to be particularly prone to spreading resistance artifacts. The earlier reports of spreading resistance effects in the (3×3)-Si reconstruction are explicitly for a 2D surface layer. Both of the materials we report here are layered van der Waals solids, somewhat similar to graphite in macroscopic characteristics. It is likely that the impact of reduced dimensionality is to strongly inhibit transport away from the injection point in the direction perpendicular to the 2D surface layer. This could enhance the relative importance of spreading resistance artifacts. In fact, the importance of considering resistivity anisotropy in nanoscale spreading resistance experiments has been addressed in the past [32,33] and will be discussed further in the next section. By contrast, the more isotropic 3D structure of the spin-orbit assisted iridates might allow such effects to be diminished compared to the rigid shifts associated with TIBB in Sr_2IrO_4 [30,40]. In this case, which shows no evidence of spreading resistance artifacts, the material exhibits lower bulk resistivity of 1–2 Ω cm compared to $RuCl_3$ (see next section), with only minor resistivity anisotropy [41].

B. Charge transport in $RuCl_3$ and $Ir_{0.5}Ru_{0.5}Cl_3$

We can view the presence of spreading resistance artifacts as transforming the tunneling experiments from a

spectroscopic probe into a local charge-transport probe. This can be seen by extracting the resistances from the linear part of the *I*-*V* curves in Figs. 4(a) and 4(b) and extrapolating them to large tunneling setpoints as shown in Fig. 5(b). An exponential fit to this dependence can be used to extract a spreading resistance of ∼1.7 GΩ for $RuCl_3$ and ∼2.8 GΩ for $Ir_{0.5}Ru_{0.5}Cl_3$. Baffou *et al.* argued that this spreading resistance measured through STS gives a way to directly measure the conductivity within the upper and lower Hubbard bands [17].

To apply this idea to $RuCl_3$ and $Ir_{0.5}Ru_{0.5}Cl_3$, we first consider previous measurements of the bulk resistivity of $RuCl_3$ that have been reported to be about 1000 Ω cm in the honeycomb plane by several groups [25,42]. However, resistivity measurements on such highly resistive, anisotropic, and often irregularly shaped samples are known to be challenging [43]. A recent study focusing on $RuCl_3$ nanoflakes reports that good electrical contacts could only be obtained by ion milling the contact region prior to metal deposition [44]. This suggests that there are significant contact resistance effects that influence resistivity measurements, which is also consistent with our recent studies of injection-limited high-bias transport properties [3]. Intriguingly, the nanoflake study [44] reported resistivity values many orders of magnitude lower than other work; 0.1 Ω cm compared to 1000 Ω cm [25,42]. This large discrepancy can be attributed to the layered nature of the material that can lead to a macroscopic lateral resistivity measurement that involves electrical contacts to different layers of the crystal and is thus not a perfectly "in-plane" probe.

Our own temperature-dependent two-contact resistivity measurements in Fig. 4(a) show strongly activated insulating characteristics but yield resistivity values notably higher than most previous reports for $RuCl_3$. At room temperature, using macroscopic sample dimensions, we observe $RuCl_3$ to have a two-contact resistivity of 2×10^5 Ω cm and $Ir_{0.5}Ru_{0.5}Cl_3$ to have a higher resistivity of 3×10^7 Ω cm. The general trend of higher resistance for Ir-substituted materials is robust and will be discussed below. Nevertheless, it is clear from comparison of the bulk and nanoscale results that the details of charge transport in strongly insulating $RuCl_3$ and related materials are highly variable across different samples and experiments.

The spreading resistance effects in STS measurements give a complementary approach to assessing charge transport in these materials. Using the values of spreading resistance extrapolated from Fig. 4, we can apply a recent theoretical analysis for layered materials to extract transport information [32,33]. An important insight is that for an anisotropic material, the spreading resistance is proportional to the geometric mean of the in-plane and out-of-plane resistivities as follows [33]:

$$R_{sp} = \frac{\sqrt{\rho_{\parallel}\rho_{\perp}}}{4r}. \tag{2}$$

In this expression, r is the radius of the injecting-point contact, $\rho_{\parallel}$ is the resistivity in the honeycomb plane, and $\rho_{\perp}$ is the resistivity perpendicular to the plane. An implication of the anisotropy is that the penetration of potential lines into the substrate occurs only over a very thin region perpendicular to the surface, and that the lateral region probed is effectively significantly larger than the point-contact geometrical area [32].

Early transport studies in $RuCl_3$ indicated a very strong anisotropy for which $\rho_{\perp}$ is more than 10^3 times larger than $\rho_{\parallel}$ [25]. Based on the spreading resistances observed in our STS studies, the geometric mean of these two quantities can be directly extracted. Assuming a radius of the injection region of 1 nm [37], the geometric mean is found to be $\sqrt{\rho_{\parallel}\rho_{\perp}} = 680$ Ω cm for $RuCl_3$ and $\sqrt{\rho_{\parallel}\rho_{\perp}} = 1120$ Ω cm for $Ir_{0.5}Ru_{0.5}Cl_3$. The earliest pair of macroscopic resistivity values [25] for pure $RuCl_3$ would give a geometric mean that is several orders of magnitude larger than we have extracted from spreading resistance extrapolation. This immediately indicates that the resistivity of the parent material is indeed poorly understood in the literature. The small values we observe cannot be consistent with the older literature values but could be consistent with the more recent nanoflake studies. These measurements have extracted $\rho_{\parallel} \sim 0.1$ Ω cm [44] and this number could be considered more accurate than bulk measurements since the electrical contacts are definitively made to a single top layer. Moreover, the very thin geometry of the flake more accurately reflects the narrow penetration depth of injected current when compared to the macroscopic thickness of bulk resistivity samples. Using this value, our experimental spreading resistance values imply a value for $\rho_{\perp} = 4.6 \times 10^6$ Ω cm for $RuCl_3$ and thus as substantially larger resistivity anisotropy than previously measured. Interestingly, this resistivity is not far from the macroscopic two-contact resistivity of our samples. This indeed suggests that the macroscopic measurements tend to probe the interlayer resistivity due to the inability to reliably contact a single layer on irregular anisotropic samples.

A broad significance of these measurements lies in understanding the impact of substitutional alloying on the Mott insulating state of $RuCl_3$. The substitution of Ir^{3+} for Ru^{3+} creates several potentially competing effects. First, the integration of heavier Ir nuclei in the solid should enhance SOC effects and thus slightly increase the SO-assisted Mott gap. Apart from this, we expect this substitution to be somewhat electronically benign in that the Ir^{3+} ions have a full t_{2g} orbital set and thus no significant impact on charge doping or local magnetic moments. However, the substitution must certainly create structural [8] and electrostatic disorder in the parent $RuCl_3$ Mott insulator. In particular, one of the major structural imperfections associated with $RuCl_3$ and its substitutional alloys is the stacking fault [8], which could substantially impact the out-of-plane resistivity $\rho_{\perp}$.

The comparison of α-$RuCl_3$ and $Ir_{0.5}Ru_{0.5}Cl_3$ via STM-based spreading resistance measurements shows relatively minor changes in charge-transport behavior due to Ir substitution. By contrast, macroscopic resistivity measurements show dramatic changes in resistivity and its temperature dependence. The comparison of the local measurements to the macroscopic measurements strongly implicates interlayer transport as the dominating factor in the latter. In particular, substitution of Ir may lead to a higher density of stacking faults that gives rise to a strong enhancement of interlayer resistivity. Thus, the effect of Ir substitution is seen to be relatively minor on a microscopic scale and can be used to control disorder within the honeycomb plane while having only minimal electronic and transport impacts.

In principle, disorder in a Mott insulator is often observed to give rise to a "soft" gap [45,46] where the insulator

becomes an unusual correlated metal. Relatedly, the incorporation of disorder could be viewed as a Mott insulator to Anderson insulator transition when the energy spread of electronic disorder is comparable in size to the Hubbard U [47]. In the large U situation of $RuCl_3$, the Mott insulating behavior cannot be readily overcome by disorder effects. It is clear from UPS and transport measurements that $Ir_{0.5}Ru_{0.5}Cl_3$ remains strongly insulating with a large gap that would not be expected in an Anderson insulator [48]. We caution that the tunneling spectra in Fig. 2 and Fig. 3 could easily be misinterpreted as evidence of a disorder-induced soft gap if the full setpoint-dependent trend was not considered from a spreading resistance perspective.

The general impact of Ir substitution is thus to maintain the strong Mott regime of $RuCl_3$ and the disorder is not sufficient to move the material into a new Anderson insulator-like phase. In the UPS measurements, the weak intensity above the band edge near 1 eV could arise from an alloy band [49] that would most likely act as a source of strongly localized charge traps. This could contribute to the increase in resistivity due to Ir substitution in addition to the expectation of increased stacking-fault defects. Most importantly, the substitution can be used to impact magnetic ordering while still maintaining the strong Mott regime of the parent material.

V. SUMMARY AND CONCLUSIONS

In this work we have resolved a known issue [12] with tunneling spectroscopy measurements of the charge gap in $RuCl_3$ by identifying spreading resistance artifacts. These artifacts broaden the spectral features and narrow the apparent gap in tunneling measurements so that they do not accurately reflect the density of states of the material. These effects can be qualitatively reproduced in a numerical model of tunneling that includes the spreading resistance in series with the tunneling resistance. In this situation, instead of a spectroscopic probe, tunneling measurements provide information about the local charge-transport properties of α-$RuCl_3$ and its substitutional alloy $Ir_{0.5}Ru_{0.5}Cl_3$ via local measurement of spreading resistance. Based on local spreading resistance measurements, these two materials are expected to have only slightly different resistivities and resistivity anisotropies. This contrasts with macroscopic measurements that show dramatic differences most likely due to differences in stacking-fault defect density in the two materials. This will prove useful in future analysis of these solid solutions for quantum materials applications.

ACKNOWLEDGMENTS

Scanning tunneling spectroscopy experiments were funded by the U.S. Department of Energy, Office of Science, Basic Energy Sciences under Award No. DE-SC0010324. The materials' synthesis was supported by funding from the National Science Foundation (Award No. 2004455). Transport experiments were funded by the U.S. Department of Energy, Office of Science, Basic Energy Sciences under Award No. DE-SC0020992.

[1] W. Witczak-Krempa, G. Chen, Y. B. Kim, and L. Balents, in Annu. Rev. Condens. Matter Phys. **5**, 57 (2014).
[2] H.-S. Kim, V. Shankar V. A. Catuneanu, and H.-Y. Kee, Phys. Rev. B **91**, 241110(R) (2015).
[3] J. R. Frick, S. Sridhar, S. O'Donnell, P. A. Maggard, and D. B. Dougherty, Appl. Phys. Lett. **116**, 183501 (2020).
[4] A. Banerjee, J. Q. Yan, J. Knolle, C. A. Bridges, M. B. Stone, M. D. Lumsden, D. G. Mandrus, D. A. Tennant, R. Moessner, and S. E. Nagler, Science **356**, 1055 (2017).
[5] Y. Kubota, H. Tanaka, T. Ono, Y. Narumi, and K. Kindo, Phys. Rev. B **91**, 094422 (2015).
[6] D. Nevola, A. Bataller, A. Kumar, S. Sridhar, J. Frick, S. O'Donnell, H. Ade, P. A. Maggard, A. F. Kemper, K. Gundogdu, and D. B. Dougherty, Phys. Rev. B **103**, 245105 (2021).
[7] S.-H. Do, C. H. Lee, T. Kihara, Y. S. Choi, S. Yoon, K. Kim, H. Cheong, W.-T. Chen, F. Chou, H. Nojiri, and K.-Y. Choi, Phys. Rev. Lett. **124**, 047204 (2020).
[8] S.-H. Do, W. J. Lee, S. Lee, Y. S. Choi, K. J. Lee, D. I. Gorbunov, J. Wosnitza, B. J. Suh, and K.-Y. Choi, Phys. Rev. B **98**, 014407 (2018).
[9] P. Lampen-Kelley, A. Banerjee, A. A. Aczel, H. B. Cao, M. B. Stone, C. A. Bridges, J. Q. Yan, S. E. Nagler, and D. Mandrus, Phys. Rev. Lett. **119**, 237203 (2017).
[10] S. Sinn, C. H. Kim, B. H. Kim, K. D. Lee, C. J. Won, J. S. Oh, M. Han, Y. J. Chang, N. Hur, H. Sato, B. G. Park, C. Kim, H. D. Kim, and T. W. Noh, Sci. Rep. **6**, 39544 (2016).
[11] L. J. Sandilands, C. H. Sohn, H. J. Park, S. Y. Kim, K. W. Kim, J. A. Sears, Y. J. Kim, and T. W. Noh, Phys. Rev. B **94**, 195156 (2016).
[12] M. Ziatdinov, A. Banerjee, A. Maksov, T. Berlijn, W. Zhou, H. B. Cao, J. Q. Yan, C. A. Bridges, D. G. Mandrus, S. E. Nagler, A. P. Baddorf, and S. V. Kalinin, Nat. Commun. **7**, 13774 (2016).
[13] J. A. Stroscio, R. M. Feenstra, and A. P. Fein, Phys. Rev. Lett. **57**, 2579 (1986).
[14] R. M. Feenstra, Phys. Rev. B **50**, 4561 (1994).
[15] M. McEllistrem, G. Haase, D. Chen, and R. J. Hamers, Phys. Rev. Lett. **70**, 2471 (1993).
[16] R. M. Feenstra, Y. Dong, M. P. Semtsiv, and W. T. Masselink, Nanotechnology **18**, 044015 (2006).
[17] G. Baffou, A. J. Mayne, G. Comtet, and G. Dujardin, Phys. Rev. B **77**, 165320 (2008).
[18] S.-Y. Park, S.-H. Do, K.-Y. Choi, D. Jang, T.-H. Jang, J. Schefer, C.-M. Wu, J. S. Gardner, J. M. S. Park, J.-H. Park, and S. Ji, arXiv:1609.05690 (2016).
[19] S. Pazoki and D. B. Dougherty, J. Chem. Phys. **151**, 214706 (2019).
[20] J. Wang, A. Deloach, W. Jiang, C. M. Papa, M. Myahkostupov, F. N. Castellano, F. Liu, and D. B. Dougherty, Phys. Rev. B **95**, 241410(R) (2017).
[21] B. Koslowski, C. Dietrich, A. Tschetschetkin, and P. Ziemann, Phys. Rev. B **75**, 035421 (2007).
[22] M. Passoni, F. Donati, A. Li Bassi, C. S. Casari, and C. E. Bottani, Phys. Rev. B **79**, 045404 (2009).

[23] A. Pronschinske, D. J. Mardit, and D. B. Dougherty, Phys. Rev. B **84**, 205427 (2011).
[24] See Supplemental Material at http://link.aps.org/supplemental/10.1103/PhysRevB.108.245410 for detailed numerical modeling methods, results, and scripts.
[25] L. Binotto, I. Pollini, and G. Spinolo, Phys. Status Solidi B **44**, 245 (1971).
[26] X. Q. Zhou, H. X. Li, J. A. Waugh, S. Parham, H. S. Kim, J. A. Sears, A. Gomes, H. Y. Kee, Y. J. Kim, and D. S. Dessau, Phys. Rev. B **94**, 161106(R) (2016).
[27] P. Mårtensson and R. M. Feenstra, Phys. Rev. B **39**, 7744 (1989).
[28] V. Ramachandran and R. M. Feenstra, Phys. Rev. Lett. **82**, 1000 (1999).
[29] H. M. Hill, A. F. Rigosi, K. T. Rim, G. W. Flynn, and T. F. Heinz, Nano Lett. **16**, 4831 (2016).
[30] I. Battisti, V. Fedoseev, K. M. Bastiaans, A. de la Torre, R. S. Perry, F. Baumberger, and M. P. Allan, Phys. Rev. B **95**, 235141 (2017).
[31] F. Flores and N. García, Phys. Rev. B **30**, 2289 (1984).
[32] E. Koren, A. W. Knoll, E. Lörtscher, and U. Duerig, Appl. Phys. Lett. **105**, 123112 (2014).
[33] K. Seki, T. Kubo, N. Ye, and T. Shimizu, Sci. Rep. **10**, 10633 (2020).
[34] V. A. Gasparov, M. Riehl-Chudoba, B. Schröter, and W. Richter, Europhys. Lett. **51**, 527 (2000).
[35] M. Grönke, P. Schmidt, M. Valldor, S. Oswald, D. Wolf, A. Lubk, B. Büchner, and S. Hampel, Nanoscale **10**, 19014 (2018).
[36] M. Berthe, R. Stiufiuc, B. Grandidier, D. Deresmes, C. Delerue, and D. Stiévenard, Science **319**, 436 (2008).
[37] P. S. N. Barimar, B. Naydenov, J. Li, and J. J. Boland, Appl. Phys. Lett. **110**, 263111 (2017).
[38] J. Dai, E. Calleja, G. Cao, and K. McElroy, Phys. Rev. B **90**, 041102(R) (2014).
[39] Q. Li, G. Cao, S. Okamoto, J. Yi, W. Lin, B. C. Sales, J. Yan, R. Arita, J. Kuneš, A. V. Kozhevnikov, A. G. Eguiluz, M. Imada, Z. Gai, M. Pan, and D. G. Mandrus, Sci. Rep. **3**, 3073 (2013).
[40] I. Battisti, K. M. Bastiaans, V. Fedoseev, A. de la Torre, N. Iliopoulos, A. Tamai, E. C. Hunter, R. S. Perry, J. Zaanen, F. Baumberger, and M. P. Allan, Nat. Phys. **13**, 21 (2017).
[41] G. Cao, J. Bolivar, S. McCall, J. E. Crow, and R. P. Guertin, Phys. Rev. B **57**, R11039(R) (1998).
[42] Y. Imai, K. Konno, Y. Hasegawa, T. Aoyama, and K. Ohgushi, Phys. Rev. B **99**, 245141 (2019).
[43] Y. Kasahara, K. Sugii, T. Ohnishi, M. Shimozawa, M. Yamashita, N. Kurita, H. Tanaka, J. Nasu, Y. Motome, T. Shibauchi, and Y. Matsuda, Phys. Rev. Lett. **120**, 217205 (2018).
[44] S. Mashhadi, D. Weber, L. M. Schoop, A. Schulz, B. V. Lotsch, M. Burghard, and K. Kern, Nano Lett. **18**, 3203 (2018).
[45] D. Heidarian and N. Trivedi, Phys. Rev. Lett. **93**, 126401 (2004).
[46] Z. Wang, Y. Okada, J. O'Neal, W. Zhou, D. Walkup, C. Dhital, T. Hogan, P. Clancy, Y.-J. Kim, Y. F. Hu, L. H. Santos, S. D. Wilson, N. Trivedi, and V. Madhavan, Proc. Natl. Acad. Sci. **115**, 11198 (2018).
[47] K. Byczuk, W. Hofstetter, and D. Vollhardt, Phys. Rev. Lett. **94**, 056404 (2005).
[48] H. Shinaoka and M. Imada, J. Phys. Soc. Jpn. **78**, 094708 (2009).
[49] D. Semmler, K. Byczuk, and W. Hofstetter, Phys. Rev. B **81**, 115111 (2010).